Study on the structural and electrical properties of YMnO$_3$ co-substituted with transition metal ions at Mn-site and their conduction mechanism

Lisham Paris Chanu[1] and Sumitra Phanjoubam[1,*]

[1] *Department of Physics, Manipur University, Canchipur, Manipur 795003, India*

ABSTRACT

Rare earth manganite YMnO$_3$ and YMn$_{0.9}$Cr$_{0.06}$Fe$_{0.04}$O$_3$ wherein transition metal ions are co-substituted at Mn-sites, were synthesized via sol–gel auto combustion route. The present work aims to study the effect of Cr^{3+} and Fe^{3+} co-substitution at Mn-site of YMnO$_3$, on their structural and electrical properties. The structural and morphological studies were performed using X-ray diffraction (XRD), Raman spectroscopy, and field emission scanning electron microscopy (FESEM). The XRD pattern confirmed the existence of monophasic hexagonal structure for YMnO$_3$ while the onset of few orthorhombic peaks was observed for YMn$_{0.9}$Cr$_{0.06}$Fe$_{0.04}$O$_3$. The A_1 Raman scattering line at ~ 676 cm^{-1} was observed to be much stronger than the other Raman modes. Uniform and dense morphological structure were observed in the FESEM micrographs. Enhanced dielectric properties were observed in the substituted sample. The frequency dependence of AC conductivity was investigated using Jonscher's law. Non-overlapping small polaron tunnelling model was predicted for the conduction model in YMnO$_3$ and correlated barrier hopping in YMn$_{0.9}$Cr$_{0.06}$Fe$_{0.04}$O$_3$ to elucidate the conduction mechanism of the system. The activation energy for intrinsic charge carriers was calculated using Arrhenius equation. The impact of grains and grain boundaries on the electrical behaviour of the samples was validated by fitting the Nyquist plot.

1 Introduction

In the past few decades, advances in materials science have led to various developments in different fields such as nanotechnology, electronic materials, biomedical technology, energy storage etc. [1]. Materials science embodies different materials from ceramics to metals, semiconductors, alloys, polymers, composites, biomaterials etc. and study of their structural, mechanical, electrical, and magnetic properties to enhance their functionalities in different fields. Various nanocomposite materials have also been developed for wide application in photocatalytic and antibacterial activities, electrolytes of solid-

Address correspondence to E-mail: sumitraphanjoubam@gmail.com

state batteries, optoelectronics, food packaging materials etc. [2–6]. Another class of nanomaterials are the multiferroics, which possess at least two or more ferroic order such as ferroelectricity, (anti-)ferromagnetism and ferroelasticity. These materials have drawn considerable interest from the research community around the world. They are potential materials for applications in transducers, sensors, actuators, memory devices, spintronics and other fields [7–13]. Rare-earth manganite ($RMnO_3$) forms one of the promising candidates for multiferroic materials due to their cross-coupling between the magnetic and electric order in a single phase [14]. Generally, they are crystallized into two structural phases, depending on the ionic size of the rare-earth elements as well as the doping element. Smaller ionic radii of the rare-earth (R = Ho–Lu, Y, and Sc) favours hexagonal structure while relatively larger ionic radii (R = La–Dy) favours the orthorhombic phase [15]. Among the rare-earth manganites, $YMnO_3$ has emerged as one of the interesting lead-free multiferroic materials due to the absence of volatile elements and for its ferroelectric property at room temperature ($T_C \sim 900$ K) [14, 16]. In $YMnO_3$ structure, each Mn^{3+} ion forms MnO_5 trigonal bipyramids with three in-plane (*ab* plane) and two apical oxygen (along *c* direction) ions separated by layers of Y^{3+} ions along the c axis. The ferroelectricity in $YMnO_3$ arises due to buckling of MnO_5 polyhedra accompanied by displacement of Y^{3+} layers while the origin of magnetism is attributed to anti-ferromagnetic superexchange interaction of Mn spins in the *ab* plane of $YMnO_3$ structure [17].

In most of the multiferroics, high leakage current, poor dielectric features and low polarisations are major drawbacks for device applications. Hence, the need to study their electrical properties and transport mechanism [18, 19]. One of the favourable ways to improve the magnetic or electrical properties of the parent compound is by substitution at Y-site or Mn-site. The substituting element also play a crucial role in tuning the properties of the parent compound. Various research works have been done on improving the properties of $YMnO_3$ by substituting various elements such as Cr, Ti, Zr, Os, Ni, Fe, Co, Mg etc. at Mn-site or Y-site [20–28]. However, detailed literature review reveals that there is limited report on the detailed study of co-substituted $YMnO_3$.

The present work, therefore, aims to investigate pristine $YMnO_3$ and the effect of co-substitution of transition metal ions Cr^{3+} and Fe^{3+} at the Mn-site on the properties of the system. Various synthesis techniques are available for fabrication of nanoparticles viz. co-precipitation, hydrothermal, sol–gel, sonochemical method etc. [29–32]. Among these synthesis techniques, sol–gel combustion has several advantages such as homogeneous mixing of the precursors, ease in process, more uniform morphology and micro-structures etc. The present samples are synthesized using sol–gel auto-combustion method.

As the mixed oxidation states and ionic radii of the doping element play a major role in tuning the electrical properties of the parent $YMnO_3$, we expect an interesting change in the electrical properties of the substituted sample. Detailed study has been done on the structural and electrical properties of the materials in different frequency and temperature ranges showing improved electrical properties. The conduction mechanisms are discussed with the support of appropriate theoretical models, providing a deeper understanding on designing such compounds for practical applications. No such work has been reported before on the co-substituted system under investigation.

2 Experimental details

2.1 Synthesis

The polycrystalline $YMnO_3$ and $YMn_{0.9}Cr_{0.06}Fe_{0.04}O_3$ are prepared by sol–gel auto-combustion technique. Stoichiometric amount of yttrium nitrate [$Y(NO_3)_3 \cdot 6H_2O$], manganese acetate [$Mn(C_2H_3O_2)_2 \cdot 9H_2O$], chromium nitrate [$Cr(NO_3)_3 \cdot 9H_2O$], and iron nitrate [$Fe(NO_3)_3 \cdot 9H_2O$] are used as precursors for the preparation of the samples. The appropriate amounts of precursors are dissolved in deionised water (DI water) with constant stirring at 100 °C. Citric acid (CA) and ethylene glycol (EG) are added into the solution such that the molar ratio of metal ions: CA: EG is equal to 1:1:2. The resulting solution is magnetically stirred for 2 h to get a homogeneous and stable solution. The temperature of the solution is raised to 150 °C to initiate gel formation, after which it is set to 300 °C leading to auto combustion of the gel. Black powdery ash is formed on completion of the combustion process, which is further calcined at 900 °C for 2 h for complete phase formation. The calcined samples are mixed with 3 wt% polyvinyl

alcohol (PVA) and pressed into circular pellets using hydraulic press by applying 100 kg/cm^2 of pressure. Finally, the pellets are sintered at 1100 °C for 5 h using conventional furnace, with a heating rate of 5 °C/min in O_2 atmosphere.

2.2 Characterization techniques

The crystalline structure and phase formation of the samples are studied using X-ray diffraction technique. Bruker X-ray diffractometer with CuK$_\alpha$ ($\lambda = 0.154$ nm) radiation source is used to record the XRD data in the range of $20° \leq 2\theta \leq 70°$ with step size of 0.02°. Structural parameters and crystallite size are determined from the XRD data. The Raman spectra of the samples are measured at room temperature in unpolarised geometry, using a Lab Ram HR evolution with excitation laser source of 532 nm. The surface morphology and microstructural investigation of the samples are studied by employing JOEL, JSM-100F field emission scanning electron microscope (FE SEM). The electrical properties of the samples are studied from dielectric, AC conductivity and impedance analysis using Agilent HP 4284A LCR Meter in the frequency range of 100 Hz to 1 MHz. The measurements are carried out at different temperatures in the range from room temperature to 200 °C with step size of 5 °C. The samples for electrical measurement are silver coated on both sides to act as electrodes for electrical conduction.

3 Results and discussion

3.1 Structural analysis

The X-ray powder diffraction pattern of the samples are depicted in Fig. 1. It is observed from the figure that pure $YMnO_3$ crystallize in single hexagonal phase with $P6_3cm$ space group without any impurity phase as confirmed with ICDD card number 00-025-1079 and the peaks are indexed to the corresponding (*hkl*) planes.

For the $YMn_{0.9}Cr_{0.06}Fe_{0.04}O_3$ sample, few orthorhombic peaks are observed (denoted by * mark on the XRD pattern) which signifies the onset of orthorhombic phase when $YMnO_3$ is substituted at Mn-site by Cr^{3+} and Fe^{3+}. The stability of the phase of a perovskite compound based on the ABO_3 formula is determined by Goldschmidt's tolerance factor (t) given
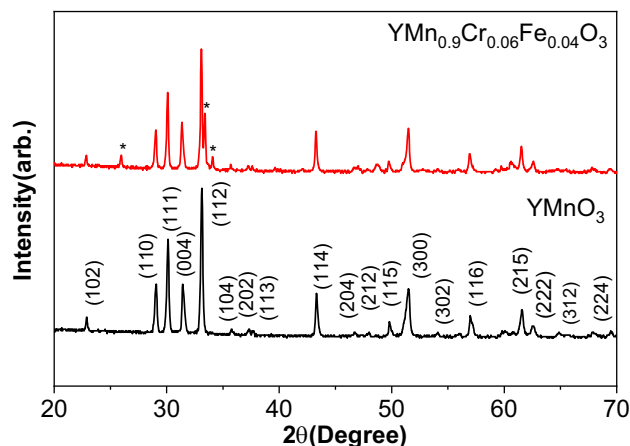

Fig. 1 X-ray diffraction patterns of $YMnO_3$ and $YMn_{0.9}Cr_{0.06}Fe_{0.04}O_3$

by, $t = \frac{(r_A + r_O)}{\sqrt{2}(r_B + r_O)}$ where, r_A, r_B and r_O represents the ionic radii of A-cation, B-cation and oxygen respectively [33]. The co-substitution at the Mn-site by ions of different size i.e., Fe^{3+} ($r_{Fe^{3+}} = 0.67$ Å) and Cr^{3+} ($r_{Cr^{3+}} = 0.61$ Å) replacing Mn^{3+}-ions ($r_{Mn^{3+}} = 0.64$ Å) causes small change in tolerance factor which may contribute to the orthorhombic phase. The average crystallite size of the samples is calculated by Scherrer equation [34],

$$D = \frac{K\lambda}{\beta \cos \theta} \qquad (1)$$

where D is the crystallite size, λ the wavelength of X-ray source, β the full width at half maximum of the diffraction peak, θ the diffraction angle in radian and K the so-called Scherrer constant. The value of K depends on the crystallite shape and the size distribution, indices of the diffraction line and the actual definition used for β [35]. It can be anywhere between 0.62 and 2.08 where in the present case $K = 0.9$ is used. The calculated value of the crystallite size only represents the estimate value and the discussion on the accuracy of Scherrer formula can be found in the literature [36].

The lattice parameters of the samples are calculated from the standard formula

$$\frac{1}{d^2} = \frac{4(h^2 + hk + k^2)}{3a^2} + \frac{l^2}{c^2} \qquad (2)$$

where d is the interplanar spacing, a and c the lattice parameter and h, k, l the Miller indices.

The calculated structural parameters and the crystallite size are tabulated in Table 1. The

crystallites are found in the nano range and the cell volume is observed to increase slightly in the substituted sample.

The FESEM micrographs of the samples are illustrated in Fig. 2 along with the histogram for particle size distribution. Uniform distribution of particles with no micro-cracks is observed for both the samples. Significant increase in particle size with uniform and dense growth of particles is observed in $YMn_{0.9}Cr_{0.06}Fe_{0.04}O_3$ with average size of 477 nm as compared to 229 nm of $YMnO_3$. The observed particle size from FESEM image is found to be very much larger as compared to the crystallite size calculated from the Scherrer equation (Table 1). It can be understood that particles are formed by aggregation of many crystallites during the sample synthesis process. Hence, calcination and sintering process of the nanopowders also contribute to the growth of larger particle size.

Raman spectroscopy is a versatile tool to study the lattice vibration of solids which can provide information on subtle local variations in the structure of the material. Figure 3 illustrates the room temperature Raman spectra of the samples fitted with Lorentzian function. Unit cell of hexagonal $YMnO_3$ with space group $P6_3cm$ consists of six formula units. Group theory calculation predicted a total of 60 phonon modes (Γ-point) for this structure viz. $10A_1 + 5A_2 + 10B_1 + 5B_2 + 15E_1 + 15E_2$ [37]. Among these modes, 38 ($9A_1 + 14E_1 + 15E_2$) are Raman active and 2 ($A_1 + 1E_1$) are infrared active while the remaining modes 20 ($5A_2 + 10B_1 + 5B_2$) are inactive or silent modes.

For pure $YMnO_3$, the experimentally observed Raman scattering bands at 676 cm^{-1} is of A_1 symmetry, 401 cm^{-1} belongs to E_1 symmetry while those at 221 cm^{-1} and 130 cm^{-1} are of E_2 symmetry. These results are in good agreement with standard reported values of Iliev et al. [38] and confirms the formation of hexagonal $YMnO_3$. In the case of $YMn_{0.9}Cr_{0.06}Fe_{0.04}O_3$ the hexagonal Raman modes are observed at 676, 397, 209, and 131 cm^{-1}. Along with these bands, orthorhombic Raman modes are also observed at 470 and 638 cm^{-1} which belong to B_{2g} Jahn–Teller symmetry in-phase oxygen stretching mode [39]. An interesting observation in the Raman spectra of both the samples is the occurrence of the most intense A_1 mode at 676 cm^{-1}. This signature mode is of substantial importance for the phonon line assignments. It can be mentioned here that a phonon mode is Raman active when its atomic displacements modulate the macroscopic polarizability. The stronger the phonon-mode-induced polarizability, the higher the intensity of the corresponding Raman line [38, 40]. This A_1 mode is related to apical oxygen atoms stretching along c-axis. The observed E_2 mode at ~ 221 cm^{-1} is associated with deformation in vibration of oxygen and Mn atoms while the band at 130 cm^{-1} is related to the motion of Y^{3+} atoms. It is observed that the E_2 mode at ~ 221 cm^{-1} and E_1 mode ~ 401 cm^{-1} of pure $YMnO_3$ are red shifted in $YMn_{0.9}Cr_{0.06}Fe_{0.04}O_3$. This is attributed to the increase in cell volume, which imply elongation of average bond length. Eventually, the force constant decrease thereby decreasing the corresponding vibrational frequency or wavenumber, which manifests as red shift in the Raman modes [41]. The red shift in peak position is also known to be attributed to local heating effects, lattice strain, microstructures, structural defects, loss of stoichiometry etc. [42].

3.2 Dielectric property

The variation of room temperature dielectric constant (ε') as a function of frequency in the range 100 Hz to 1 MHz is depicted in Fig. 4a. Usual dispersive behaviour of dielectric constant is observed in both the samples where the value is much higher at lower frequencies, decreases with increasing frequency of the applied alternating field and becomes almost constant at higher frequencies. This can be explained considering the four types of polarization

Table 1 Structural data for $YMnO_3$ and $YMn_{0.9}Cr_{0.06}Fe_{0.04}O_3$

Composition	Lattice parameters (Å)		Cell volume (Å^{-3})	Crystallite size (nm)	X-ray density, d (g cm^{-3})
	a	c	V		
$YMnO_3$	6.145	11.361	371.564	43	5.154
$YMn_{0.9}Cr_{0.06}Fe_{0.04}O_3$	6.148	11.391	372.851	53	5.132

Fig. 2 FESEM micrographs and histograms of particle size with corresponding derivatives of the cumulative distribution of **a** $YMnO_3$, and **b** $YMn_{0.9}Cr_{0.06}Fe_{0.04}O_3$
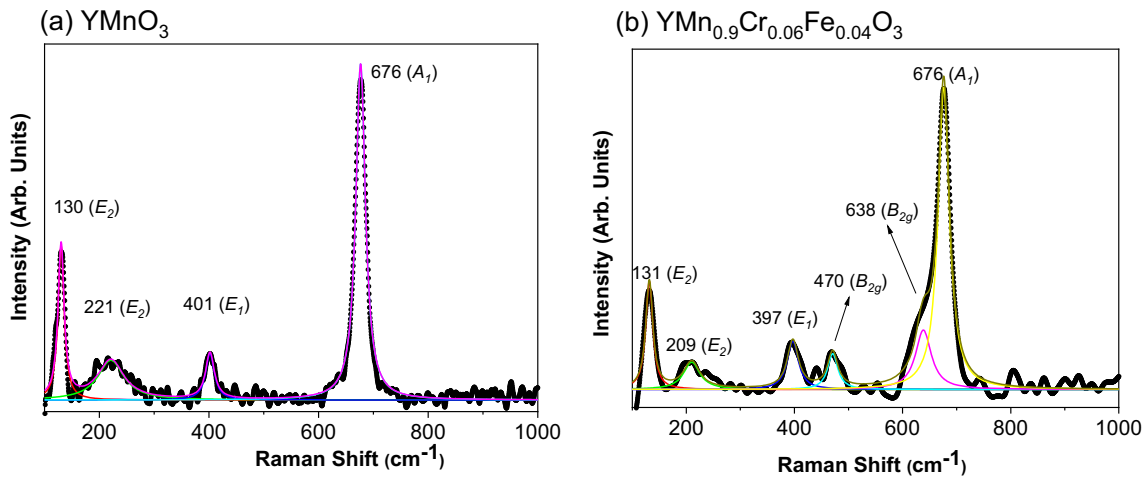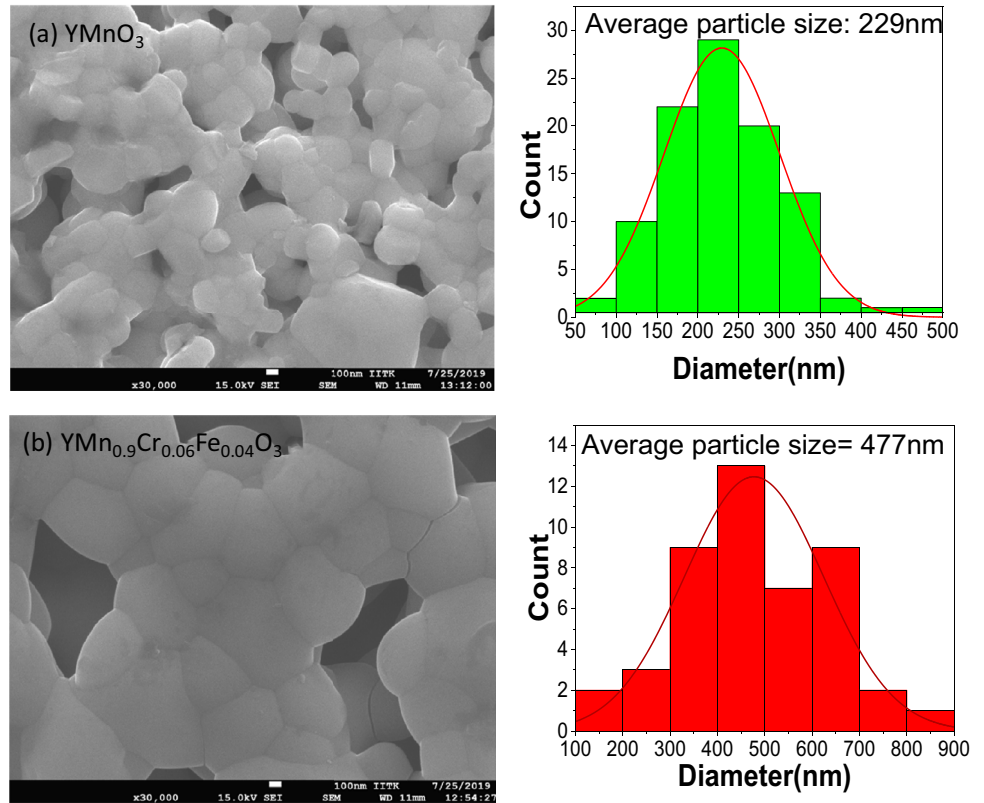

Fig. 3 Raman spectra for **a** $YMnO_3$ and **b** $YMn_{0.9}Cr_{0.06}Fe_{0.04}O_3$

phenomena viz. (1) interfacial (space-charge polarization), (2) orientational or dipolar polarization, (3) ionic polarization and (4) electronic polarization. Ionic and electronic polarization becomes significant only at very high frequency ($\sim 10^{11}$ Hz) and hence are not relevant in the frequency range of the present study. At lower frequencies, space-charge polarization and dipolar polarization contribute to the dielectric constant. The polarization in manganites is

via the electron hopping between Mn^{3+} and Mn^{4+} ions. The low frequency dispersive behaviour of dielectric constant can be well understood from Maxwell–Wagner polarization phenomena in accordance with Koop's phenomenological theory [43–45]. According to this theory, the polycrystalline materials are assumed to be composed of well-defined conducting grains surrounded by poorly conducting grain boundaries. The grain boundaries, thus, act as
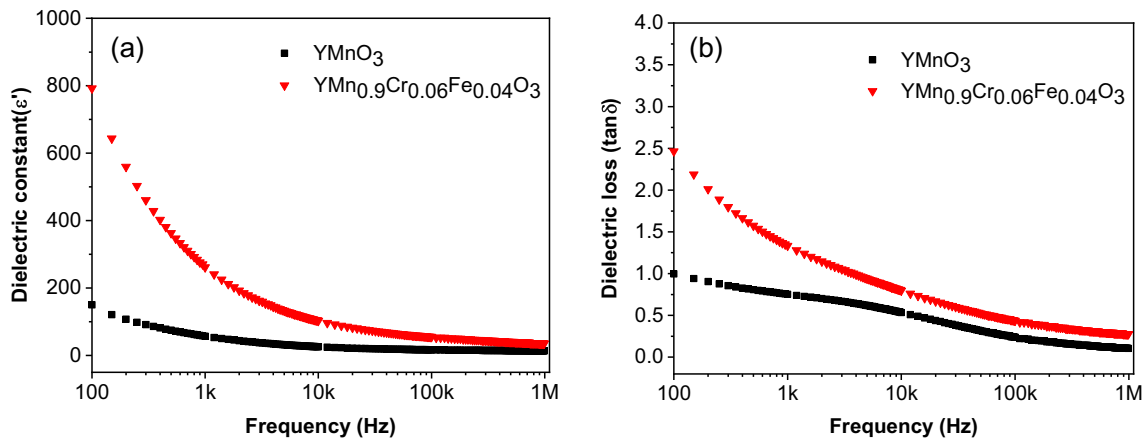
Fig. 4 Frequency dependence of **a** dielectric constant and **b** dielectric loss at room temperature

potential barrier and block the mobile charge carriers, thereby inhibiting charge hopping. Thus, mobile charge carriers get accumulated at the boundaries due to restriction of charge hopping on application of an alternating electric field. This led to localised accumulation of charges at the boundaries leading to space charge polarization and producing a very large capacitance, and hence, a large dielectric constant. As the frequency is increased, the charge carriers reverse their orientation more frequently before reaching the grain boundary and, as a consequence polarization decreases. At higher frequencies, the charge transfer could not follow the frequency of the applied field and hence the dielectric constant drops to nearly constant values.

It is also observed that the dielectric constant significantly increases with substitution of Cr^{3+} and Fe^{3+} at Mn-site. This suggest that substitution of Cr^{3+} and Fe^{3+} may induce increased transformation of Mn^{3+} to Mn^{4+} ions increasing charge hopping and hence the dielectric constant. The increase in grain size as well as uniformity of grain size may also lead to increased dielectric constant. Other factors such as lattice distortion, oxygen vacancy and creation of defect site due to doping might also influence the dielectric constant of the material [46].

Figure 4b shows the room temperature frequency variation of dielectric loss of the samples. The dielectric loss (tan δ) is observed to be very small and decrease continuously with increasing frequency and becomes almost constant at higher frequencies signifying the usual dispersive behaviour. The decrease in tan δ with frequency can be understood in

accordance with Koop's phenomenological theory as discussed above.

The temperature dependence of dielectric constant (ε′) at some selected frequencies are shown in Fig. 5a, b. It can be noticed that ε′ increases with temperature for both the samples. This indicates the presence of thermally activated charge carriers whose mobility towards the grain boundaries increase with temperature, thereby increasing space-charge polarization and hence the dielectric constant. It is also observed that as a function of frequency the temperature dependence of ε′ is strong at lower frequency but as the frequency increases, ε′ becomes almost temperature independent which may be due to the dominance of dipolar polarization over the space charge polarization at higher frequencies [47].

The temperature variation of dielectric loss at selected frequencies are shown in Fig. 5c, d. The tan δ value is found to increase with increase in temperature for all the samples and the variation exhibits similar nature as that of the variation of dielectric constant with temperature. The observed behaviour may be attributed to the accumulation of charge carriers at the grain boundaries, due to increased mobility of the ions at higher temperature, as explained above [48]. Another factor of higher dielectric loss at high temperature may be due to conduction loss, according to which the movement of ions over large distance led to loss of electric energy as some of their energy are transferred to the lattice as heat energy. As the temperature increases, the conduction loss become more pronounced due to increase of the mobility of ions, thus increasing the dielectric loss at high temperature [49].
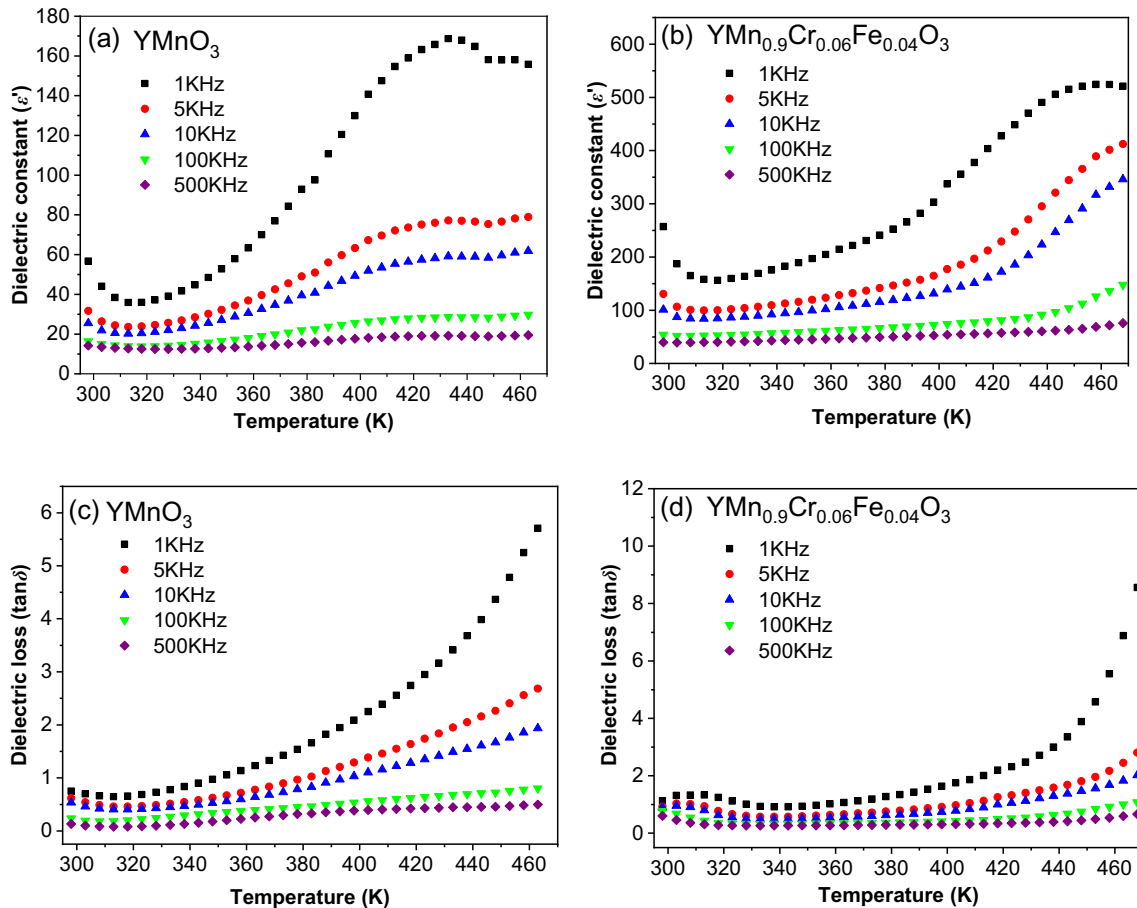
Fig. 5 a, **b** Temperature dependence of dielectric constant and **c**, **d** dielectric loss at some selected frequencies for $YMnO_3$, and $YMn_{0.9}Cr_{0.06}Fe_{0.04}O_3$

3.3 AC conductivity

The AC conductivity of the samples are investigated to have a deeper understanding on the conduction mechanism of the materials. AC conductivity (σ_{AC}) is calculated from the empirical relation

$$\sigma_{AC} = \omega\varepsilon_o\varepsilon' \tan\delta \tag{3}$$

where ε_o is the absolute permittivity (8.854×10^{-12} $C^2\ N^{-1}\ m^{-2}$), ω the angular frequency, ε' the dielectric constant and $\tan\delta$ the dielectric loss. The plot of σ_{AC} versus frequency at selected temperatures is shown in Fig. 6. It is observed that in low frequency region, the AC conductivity is small due to polarization effect (charge accumulation at grain boundaries) and at high frequency region, it increases due to hopping of charge carriers.

The AC conductivity curves are fitted by using Jonscher's Universal power law [50] which is related to the dynamics of ionic hopping transport between localised sites and is given by

$$\sigma(f) = \sigma_{dc} + Af^{n(T)} \tag{4}$$

where σ_{dc} is the dc conductivity, A a frequency dependent parameter and $n(T)$ a constant which gives the degree of interaction between the mobile ions and lattices. For $n < 1$, translational hopping of charge carriers is indicated but for $n > 1$, the motion is a localised one [51]. It is well known that the appropriate conduction mechanism can be assigned to the material from the trend of variation of frequency exponent n w.r.t. temperature. Several investigations suggested that if n is independent of temperature the electrical transport mechanism in the system is given by the quantum mechanical tunnelling model (QMT). If n increases with temperature the non-overlapping small polaron tunnelling (NSPT) can be expected for the conductivity mechanism. Whereas, correlated barrier hopping (CBH) model is
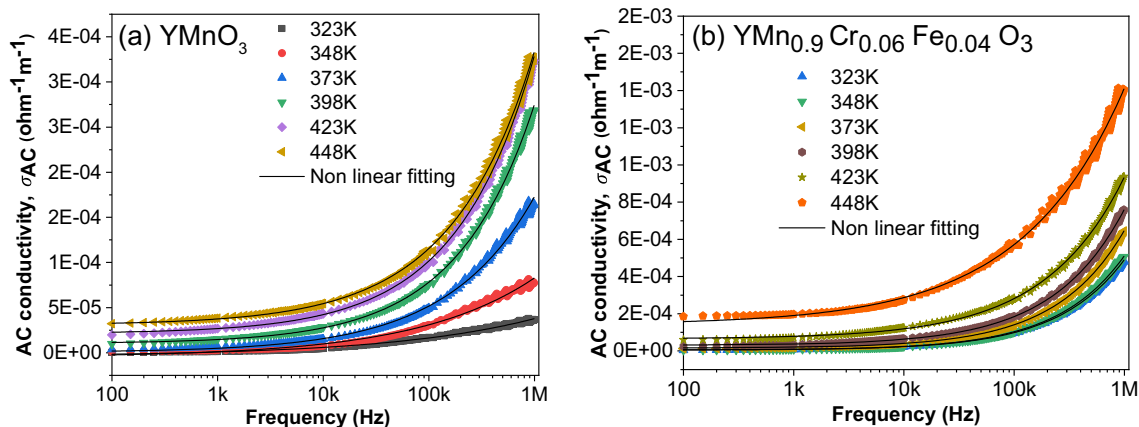
Fig. 6 Frequency variation of AC conductivity at selected temperatures for **a** $YMnO_3$ and **b** $YMn_{0.9}Cr_{0.06}Fe_{0.04}O_3$

the dominant conduction process when n decreases with temperature [52–54]. Figure 7 shows that the value of n for $YMnO_3$ increases with temperature up to 400 K, implying the NSPT conduction model for that temperature range, and then slightly decreases with temperature above 400 K, indicating the possibility of another mechanism. For $YMn_{0.9}Cr_{0.06}Fe_{0.04}$-$O_3$, the decreasing trend of n with temperature suggests that the CBH model is the most appropriate conduction model.

According to the NSPT model the frequency exponent n is given by [52–54]

$$n = 1 - \frac{4}{\left[\left(\frac{1}{\omega \tau_0} \right) - \left(\frac{W_H}{k_B T} \right) \right]} \tag{5}$$

where W_H is the barrier height or polaron energy, τ_0 relaxation time which is in the order of vibrational period (10^{-13} s) and ω is the angular frequency.

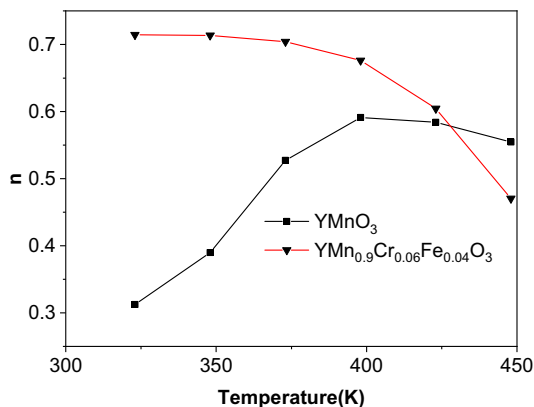For large value of $\frac{W_H}{k_B T}$, the frequency exponent becomes

Fig. 7 Variation of frequency exponent 'n' with temperature

$$n = 1 - \frac{4}{\left(\frac{W_H}{k_B T} \right)} \tag{6}$$

Using this equation, the energy of polarons has been estimated to be around 0.09 eV for $YMnO_3$.

In CBH model of conduction, the exponent n can be represented by

$$n = 1 - \frac{6 k_B T}{W_m + k_B T \ln(\omega \tau_0)} \tag{7}$$

where W_m is the maximum barrier jump height i.e., the energy required for the electron to hop from one site to another. At high value of the reduced energy $\frac{W_m}{k_B T}$, the equation is simplified as

$$n = 1 - \frac{6 k_B T}{W_m} \tag{8}$$

The barrier height for the hopping of charge is deduced from the above equation (Eq. 8) to be around 0.56 eV for $YMn_{0.9}Cr_{0.06}Fe_{0.04}O_3$.

Figure 8 shows the variation of AC conductivity (σ_{AC}) with inverse temperature $10^3/T$ (K^{-1}) at different frequencies for $YMnO_3$ and $YMn_{0.9}Cr_{0.06}$-$Fe_{0.04}O_3$. The curves are seen to consist of two regions with different slopes- region I (low temperature region) and region II (high temperature region). In region I there is strong frequency dispersion of AC conductivity for both the samples, where conductivity increases with increase in frequency. This may be attributed to hopping of charge carriers to random sites having variable barrier heights and separation [55]. While, in region II the AC conductivity curve tend to converge at high temperature, which indicates that at high temperature thermal activation of
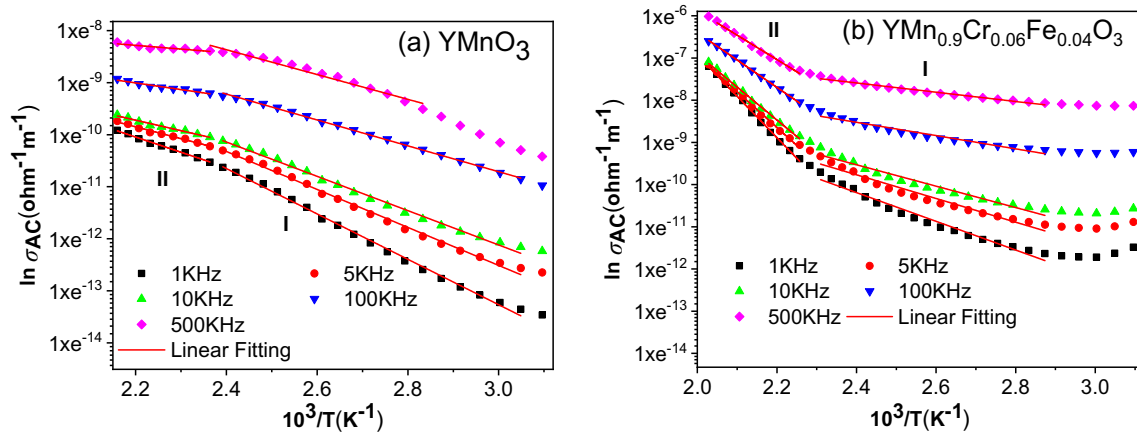
Fig. 8 Variation of AC conductivity (σ_{AC}) with inverse temperature ($10^3/T$) at selected frequencies for **a** YMnO$_3$ and **b** YMn$_{0.9}$Cr$_{0.06}$Fe$_{0.04}$O$_3$

charge carriers is dominant over the frequency dependence [56].

The activation energy is calculated by using the Arrhenius equation [57]

$$\sigma_{AC} = \sigma_0 e^{\frac{-E_a}{kT}} \tag{9}$$

where E_a is the activation energy for the intrinsic conduction of charge carriers, k the Boltzmann constant and T the temperature, and tabulated in Table 2 for the two temperature regions at different frequencies. A decrease is observed with increasing frequency.

In perovskite compounds charge carriers (electron) and oxygen vacancies generated during high temperature calcination and sintering process play a major role on the conduction behaviour. Rao et al. also reported that the valence change from Mn^{3+} to Mn^{4+} during heat treatment in YMnO$_3$ is compensated by holes (oxygen vacancies) and thus yielding p-type conductivity [58]. The created oxygen vacancies may be singly or doubly ionised according to the Kröeger–Vink notation [59],

$$V^o \Longleftrightarrow V_o' + e'; \quad V_o' \Longleftrightarrow V_o'' + e'$$
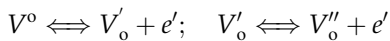
where V_o' and V_o'' are singly and doubly ionized oxygen vacancies, respectively. These holes are bound to Mn^{3+} as Mn$^{3+} + V_o' \Longleftrightarrow$ Mn^{4+} and thus the charge transfer takes place between these neighbouring Mn-ions.

The obtained activation energy values for YMnO$_3$ in both the regions and for YMn$_{0.9}$Cr$_{0.06}$Fe$_{0.04}$O$_3$ in region I indicate that the conduction is due to short range hopping motion of oxygen vacancies [60]. The larger activation energy values (0.50–0.84 eV) at different frequencies in Region II for YMn$_{0.9}$Cr$_{0.06}$Fe$_{0.04}$O$_3$ suggests that the conduction mechanism may be due to the presence of long-range motion of electrons from doubly ionized oxygen vacancies and the presence of charged defects [61, 62].

3.4 Impedance analysis

Impedance spectroscopy provides insights to the electrical conductivity behaviour and contribution of grain and grain boundaries on the electrical property of the material. The complex impedance Z* is composed of real and imaginary parts as given below

Table 2 Activation energy obtained from Arrhenius fitting of temperature variation of AC conductivity versus temperature $10^3/T$ (K^{-1}) of YMnO$_3$ and YMn$_{0.9}$Cr$_{0.06}$Fe$_{0.04}$O$_3$

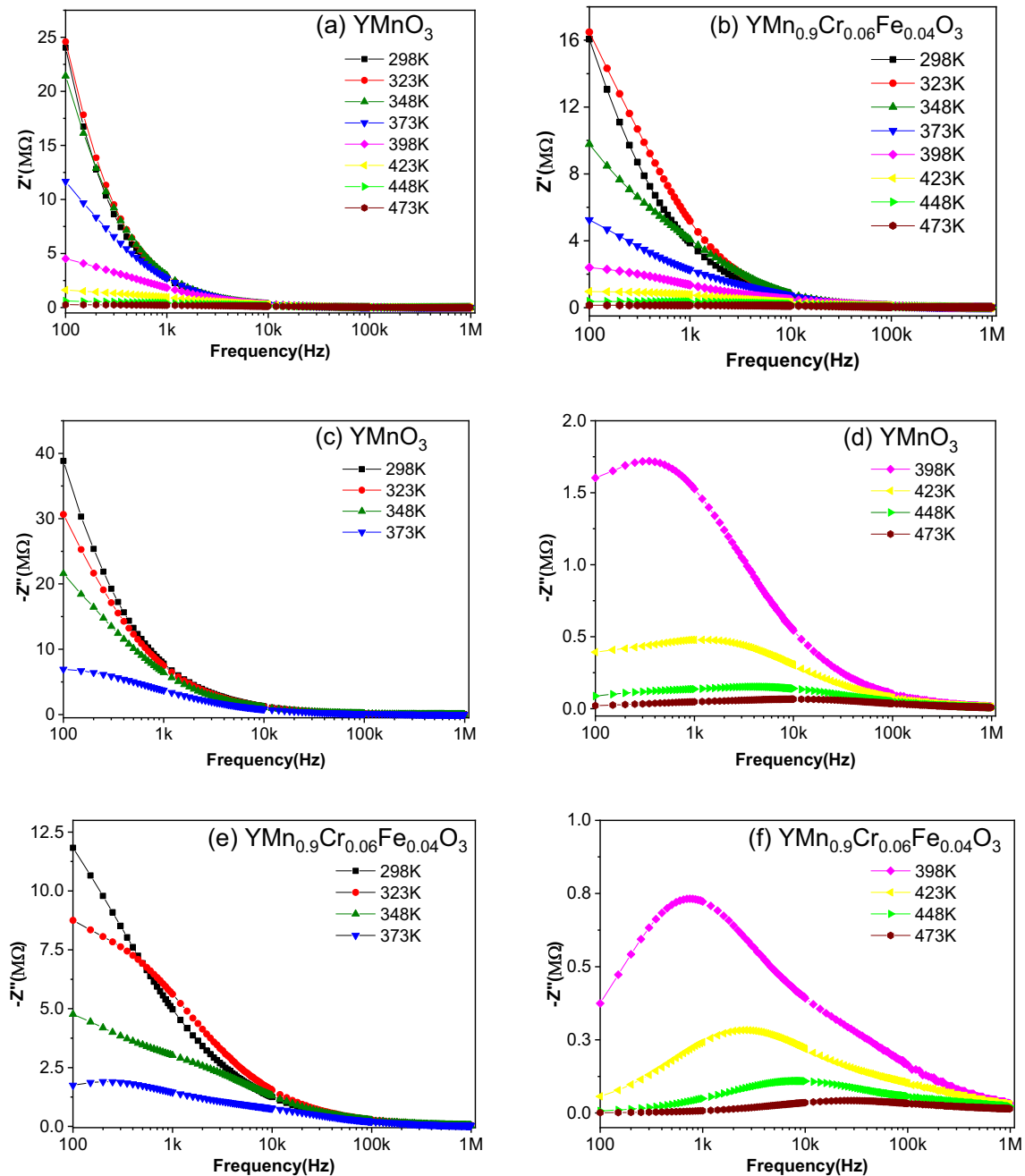| Frequency (kHz)	E_a (eV): YMnO$_3$		E_a (eV): YMn$_{0.9}$Cr$_{0.06}$Fe$_{0.04}$O$_3$	
	Region I	Region II	Region I	Region II
1	0.38	0.25	0.29	0.84
5	0.32	0.20	0.24	0.73
10	0.28	0.17	0.22	0.67
100	0.21	0.11	0.14	0.56
500	0.20	0.06	0.09	0.50

Fig. 9 **a**, **b** Variation of real part of impedance, Z' with frequency at some selected temperatures for $YMnO_3$ and $YMn_{0.9}Cr_{0.06}Fe_{0.04}O_3$ and **c**–**f** Variation of imaginary part of impedance, Z'' with frequency at some selected temperatures for $YMnO_3$ and $YMn_{0.9}Cr_{0.06}Fe_{0.04}O_3$

$$Z^* = Z' - jZ''$$
$$Z' = |Z|\cos\theta, Z'' = |Z|\sin\theta \text{ and } \omega = 2\pi f$$

where Z', Z'', and ω are the real and imaginary part of the impedance, and angular frequency, respectively.

Figure 9a, b shows the frequency dependence of the real part of impedance (Z') at different

temperatures of the studied samples. It is observed that Z' value decrease with increasing frequency and at very high frequencies (around 10 KHz) the Z' values merge for all temperatures. The decrease with frequency can be related to space charge polarization. It is also observed that as a function of temperature, Z' decreases with increase in temperature i.e., Z' is inversely proportional to temperature suggesting a
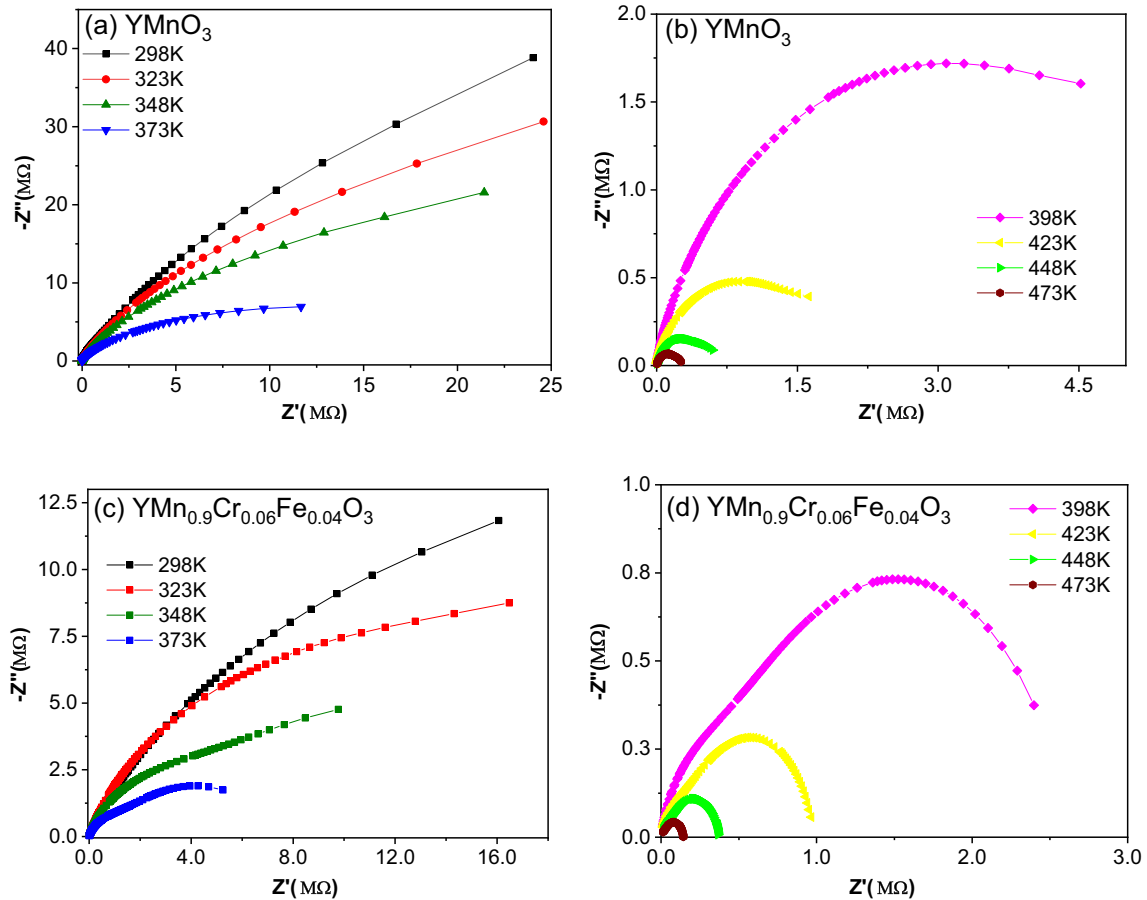
Fig. 10 Variation of Z' vs Z'' or Cole–Cole plot at selected temperatures for **a, b** YMnO$_3$ and **c, d** YMn$_{0.9}$Cr$_{0.06}$Fe$_{0.04}$O$_3$
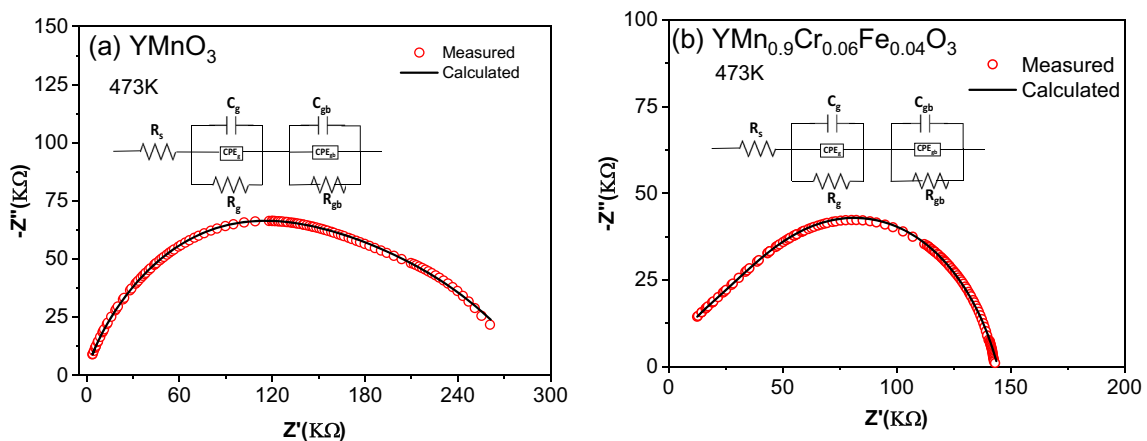

Fig. 11 An equivalent circuit fit of the Cole–Cole plot for **a** YMnO$_3$ and **b** YMn$_{0.9}$Cr$_{0.06}$Fe$_{0.04}$O$_3$ at 473 K

negative temperature coefficient of resistance (NTCR) [56]. This indicates that AC conductivity increases with temperature due to enhancement of thermally activated charge conduction which is analogous to semiconductor nature. Further, the value of Z' is less in the co-substituted sample.

The variation of Z'' vs frequency at different temperatures are shown in Fig. 9c–f. It is observed from the plot that Z'' decreases with frequency and merged at higher frequencies (above 10 KHz) for the different temperatures. The characteristic peaks of the relaxation behaviour are observed clearly at higher

Table 3 The grain and grain boundary contribution evaluated after fitting of impedance data for $YMnO_3$ and $YMn_{0.9}Cr_{0.06}Fe_{0.04}O_3$ at 473 K

Sample	$YMnO_3$	$YMn_{0.9}Cr_{0.06}Fe_{0.04}O_3$
R_s (Ω)	5.13×10^3	1.12×10^5
R_g (Ω)	8.84×10^5	4.78×10^4
CPE_g	43.5×10^{-7}	17.5×10^{-7}
C_g (F)	2.35×10^{-11}	97.1×110^{-8}
R_{gb} (Ω)	1.01×10^6	5.52×10^4
CPE_{gb}	1.43×10^{-11}	80.7×10^{-8}
C_{gb} (F)	10.9×10^{-6}	79.6×10^{-8}

temperature (~ 398 K) for both the samples which indicates the presence of relaxation phenomena. It can also be seen from the figure that the position of the peak shifts towards higher frequencies with increase in temperature which suggest that the relaxation process is temperature dependent [63].

To study the contributions of electrode interfaces, grain and grain boundary to the relaxation process of the samples, the Cole–Cole or Nyquist plot ($- Z''$ vs Z') at various selected temperature are given in Fig. 10a–d.

The Nyquist plot show characteristic incomplete semi-circular arc at lower temperatures for both the samples which indicates the high insulating behaviour. The semi-circular arc become fuller or complete with increase in temperature while the height of the peak decreases. With further increase in temperature the radius of the semi-circular arc decreases. This indicates that the conductivity of the samples increase with temperature indicting the semiconducting behaviour of the samples [64]. It can be seen that the centre of the semi-circular arcs tends to move towards the lower resistance value with increase in temperature. Moreover, the arcs are asymmetric and the centre of the arc shifts below the real part of the impedance axis which indicates the non- Debye type of relaxation process in the studied compounds [65]. The Nyquist plot are fitted using *ZSimpWin* Software to represent the multi-relaxation behaviour of the compounds in terms of a series and parallel combination of resistance and capacitance i.e., RC equivalent circuit. For non-Debye-type system, constant phase element (CPE) is introduced in the circuit [66]. The fitted impedance data along with the circuit model for the samples at 473 K are shown in Fig. 11

and the obtained fitted parameters are shown in Table 3.

The term R_s denotes the series resistance, which may be attributed to the material's electrode effect. The resistance, constant phase element, and capacitance of the grain are represented by R_g, CPE_g, and C_g, respectively while R_{gb}, CPE_{gb} and C_{gb} represent the corresponding terms for grain boundary. The goodness of fitting (χ^2) is in the order of 10^{-4} for both the samples which shows that the circuit model is fitted well with the impedance data. From the interpretation of the fitted equivalent circuit, it can be concluded that two relaxation behaviours due to grains and grain boundaries are present in both the samples. Grains boundaries are observed to be more resistive than grains in both the samples. Also, the resistance of grain and grain boundary decreases in $YMn_{0.9}Cr_{0.06}Fe_{0.04}O_3$.

4 Conclusion

Pure $YMnO_3$ and $YMn_{0.9}Cr_{0.06}Fe_{0.04}O_3$ have been synthesised via sol–gel method. X-ray diffraction confirms the formation of single hexagonal structure for $YMnO_3$ while few peaks of orthorhombic phase are observed for the co-substituted sample. Raman scattering line at ~ 676 cm^{-1} dominates the Raman spectra in both the samples. In the substituted sample, red shift of some of the Raman modes are observed which has been attributed to variation in Mn–O bond length. Significant enhancement of dielectric constant is observed in $YMn_{0.9}Cr_{0.06}Fe_{0.04}O_3$. Temperature dependence of the dielectric property predicts the thermally activated charge conduction process. The variation of the frequency exponent n with temperature in the frequency dependent AC conductivity study at different temperature indicates that the charge transport mechanism in $YMnO_3$ and $YMn_{0.9}Cr_{0.06}Fe_{0.04}O_3$ can be taken to be governed by NSPT and CBH model, respectively. The values of activation energies of the intrinsic charge carriers indicate that the conduction process in the samples are controlled by oxygen vacancies—short range motion in $YMnO_3$ and long range motion in co-substituted sample in the high temperature region. The impedance analysis shows non-Debye relaxation type in the studied samples. The fitting of Nyquist plot reveals the contribution of grain and grain boundary on the electrical behaviour.

The grain boundaries are found to be more resistive than the grains in both the sample. The obtained results can be useful for synthesizing high dielectric multiferroics for potential application in resonators and switching devices.

Author contributions

All the authors contributed to the study conception and design. Material synthesis, data collection and original draft preparation were performed by LPC. Design of the experiment and analysis of the results was done by LPC and SP. Reviewing and editing the manuscript were done by SP. All the authors read and approved the final manuscript.

Data availability

During the reviewing process, the experimental data associated with this manuscript, if needed, will be made available on request.

Code availability

Not applicable.

Declarations

Conflicts of interest The authors declare that they have no conflict of interest.

Ethical approval Not applicable.

Consent to participate Not applicable.

Consent for publication All the authors approve the submission of the manuscript in its current form.

References

1. D.D.L. Chung, *Applied Materials Science: Applications of Engineering Materials in Structural, Electronics, Thermal, and Other Industries* (CRC Press, Washington, 2001)
2. S.R. Yousefi, H.A. Alshamsi, O. Amiri, M. Salavati-Niasari, J. Mol. Liq. **337**, 116405 (2021)
3. A.M. Hezma, A. Rajeh, M.A. Mannaa, Colloids Surf. A Physicochem. Eng. Asp. **581**, 123821 (2019)
4. A. Rajeh, H.M. Ragab, M.M. Abutalib, J. Mol. Struct. **1217**, 128447 (2020)
5. S.R. Yousefi, M. Masjedi-Arani, M.S. Morassaei, M. Salavati-Niasari, H. Moayedi, Int. J. Hydrog. Energy **44**, 24005 (2019)
6. Q.A. Alsulami, A. Rajeh, Opt. Mater. **11**, 2021 (1820)
7. M. Fiebig, J. Phys. D: Appl. Phys. **38**, R123 (2005)
8. W. Prellier, M.P. Singh, P. Murugavel, J. Phys.: Condens. Matter **17**, R803 (2005)
9. C.-W. Nan, G. Liu, Y. Lin, H. Chen, Phys. Rev. Lett. **94**, 197203 (2005)
10. N.A. Spaldin, MRS Bull. **42**, 385 (2017)
11. Y. Yamasaki, S. Miyasaka, Y. Kaneko, J.-P. He, T. Arima, Y. Tokura, Phys. Rev. Lett. **96**, 207204 (2006)
12. J. Park, S. Lee, M. Kang, K.-H. Jang, C. Lee, S.V. Streltsov, V.V. Mazurenko, M.V. Valentyuk, J.E. Medvedeva, T. Kamiyama, J.-G. Park, Phys. Rev. B **82**, 054428 (2010)
13. D.I. Khomskii, J. Magn. Magn. Mater. **306**, 1 (2006)
14. A.B. Van Aken, T.T.M. Palstra, A. Filippetti, N.A. Spaldin, Nat. Mater **3**, 164 (2004)
15. H. Schmid, Ferroelectrics **162**, 317 (1994)
16. M. Kumar, D.M. Phase, R.J. Choudhary, Heliyon **5**, e01691 (2019)
17. P.J. Brown, T. Chatterji, J. Phys.: Condens. Matter **18**, 10085 (2006)
18. K.F. Wang, J.-M. Liu, Z.F. Ren, Adv. Phys. **58**, 321 (2009)
19. A.K. Pradhan, K. Zhang, D. Hunter, J.B. Dadson, G.B. Loiutts, P. Bhattacharya, R. Katiyar, J. Zhang, D.J. Sellmyer, U.N. Roy, Y. Cui, A. Burger, J. Appl. Phys. **97**, 093903 (2005)
20. O. Polat, M. Coskun, F.M. Coskun, Z. Durmus, M. Caglar, A. Turut, J. Alloys Compd. **752**, 274 (2018)
21. A. Durán, G. Guzmán, C.I. Ochoa-Guerrero, C. Herbert, R. Escudero, F. Morales, R. Escamilla, J. Appl. Phys. **125**, 034102 (2019)

22. K.N. Rathod, K. Gadani, Z. Joshi, D. Dhruv, A.D. Joshi, K. Asokan, P.S. Solanki, N.A. Shah, Mater. Today: Proc. **5**, 9804 (2018)

23. Z.L. Moreno Botello, A. Caneiro, P. Roussel, G. Gauthier, J. Alloys Compd. **690**, 348 (2017)

24. F. Wan, X. Bai, K. Song, X. Lin, X. Han, J. Zheng, C. Cao, J. Magn. Magn. Mater. **424**, 371 (2017)

25. F. Wan, X. Bai, K. Song, X. Han, J. Zheng, X. Lin, C. Cao, J Mater Sci: Mater Electron **28**, 15819 (2017)

26. S. Namdeo, A.K. Sinha, M.N. Singh, A.M. Awasthi, J. Appl. Phys. **113**, 104101 (2013)

27. O. Peña, M. Bahout, Y. Ma, T. Guizouarn, D. Gutiérrez, P. Durán, C. Moure, Mater. Sci. Eng. B **104**, 126 (2003)

28. K. Asokan, Y.S. Chen, C.W. Pao, H.M. Tsai, C.W.O. Lee, C.H. Lin, H.C. Hsueh, D.C. Ling, W.F. Pong, J.W. Chiou, M.-H. Tsai, O. Peña, C. Moure, Appl. Phys. Lett. **95**, 131901 (2009)

29. S.R. Yousefi, A. Sobhani, M. Salavati-Niasari, Adv. Powder Technol. **28**, 1258 (2017)

30. Q.A. Alsulami, A. Rajeh, M.A. Mannaa, S.M. Albukhari, D.F. Baamer, Int. J. Hydrog. Energy **46**, 27349 (2021)

31. S. Raheleh Yousefi, A. Sobhani, H. Abbas Alshamsi, M. Salavati-Niasari, RSC Adv. **11**, 11500 (2021)

32. M.M. Abutalib, A. Rajeh, Polym. Test. **93**, 107013 (2021)

33. V.M. Goldschmidt, Naturwissenschaften **14**, 477 (1926)

34. P. Scherrer, Nachr. Ges. Wiss. Göttingen. Math. Phys. Klasse **2**, 96–100 (1918)

35. J.I. Langford, A.J.C. Wilson, J. Appl. Cryst. **11**, 102 (1978)

36. V. Uvarov, I. Popov, Mater. Charact. **85**, 111 (2013)

37. A.L. Rousseau, R.P. Bauman, S.P.S. Porto, J. Raman Spectrosc. **10**, 253 (1981)

38. M.N. Iliev, H.-G. Lee, V.N. Popov, M.V. Abrashev, A. Hamed, R.L. Meng, C.W. Chu, Phys. Rev. B **56**, 2488 (1997)

39. M.N. Iliev, M.V. Abrashev, H.-G. Lee, V.N. Popov, Y.Y. Sun, C. Thomsen, R.L. Meng, C.W. Chu, Phys. Rev. B **57**, 2872 (1998)

40. A. Varshney, P. Sharma, A. Kumar, Mater. Res. Express **2**, 076102 (2015)

41. J. Shukla, A. Mishra, J. Supercond. Nov. Magn. **34**, 451 (2021)

42. H. Fukumura, S. Matsui, H. Harima, K. Kisoda, T. Takahashi, T. Yoshimura, N. Fujimura, J. Phys.: Condens. Matter **19**, 365239 (2007)

43. J.C. Maxwell, *A Treatise on Electricity and Magnetism* (Clarendon Press, Oxford, 1873)

44. A. Wagner, Arch. Elektroteeh **3**, 83 (1914)

45. A.G. Koops, Phys. Rev. **83**, 121 (1951)

46. S. Zheng, D. Shi, L. Liu, G. Li, Q. Wang, L. Fang, B. Elouadi, J Mater Sci: Mater Electron **25**, 4058 (2014)

47. L.L. Hench, J.K. West, *Principles of Electronic Ceramics* (Wiley, New York, 1990)

48. P.R. Das, L. Biswal, B. Behera, R.N.P. Choudhary, Mater. Res. Bull. **44**, 1214 (2009)

49. J.M. Stevels, *Electrical Conductivity II/Elektrische Leitungsphänomene II* (Springer, Berlin, 1957), p. 350

50. A.K. Jonscher, Nature **267**, 673 (1977)

51. A.N. Papathanassiou, I. Sakellis, J. Grammatikakis, Appl. Phys. Lett. **91**, 122911 (2007)

52. A. Ghosh, Phys. Rev. B **41**, 1479 (1990)

53. S.R. Elliott, Philos. Mag. **36**, 1291 (1977)

54. S. Nasri, A.L.B. Hafsia, M. Tabellout, M. Megdiche, RSC Adv. **6**, 76659 (2016)

55. P. Pandit, S. Satapathy, P.K. Gupta, Phys. B: Condens. Matter **406**, 2669 (2011)

56. T. Sahu, B. Behera, J Mater Sci: Mater Electron **29**, 7412 (2018)

57. K.J. Laidler, J. Chem. Educ. **61**, 494 (1984)

58. G.V.S. Rao, B.M. Wanklyn, C.N.R. Rao, *Solid State Chemistry* (World Scientific, Singapore, 1995), pp. 365–378

59. R.E. Cook, K.C. Goretta, J. Wolfenstine, P. Nash, J.L. Routbort, Acta Mater. **47**, 2969 (1999)

60. P.R. Mandal, T.K. Nath, J. Alloys Compd. **628**, 379 (2015)

61. M. Bourguiba, Z. Raddaoui, A. Dhari, M. Chafra, J. Dhahri, M.A. Garcia, J Mater Sci: Mater Electron **31**, 11810 (2020)

62. A. Rehman, J.-B. Li, J.-S. Zhang, M. Rizwan, C. Niu, H.-B. Jin, J. Appl. Phys. **118**, 214101 (2015)

63. T. Sahu, B. Behera, J. Phys. Chem. Solids **113**, 186 (2018)

64. M. Younas, M. Nadeem, M. Atif, R. Grossinger, J. Appl. Phys. **109**, 093704 (2011)

65. M. Smari, H. Rahmouni, N. Elghoul, I. Walha, E. Dhahri, K. Khirouni, RSC Adv. **5**, 2184 (2014)

66. R. Schmidt, W. Eerenstein, T. Winiecki, F.D. Morrison, P.A. Midgley, Phys. Rev. B **75**, 245111 (2007)